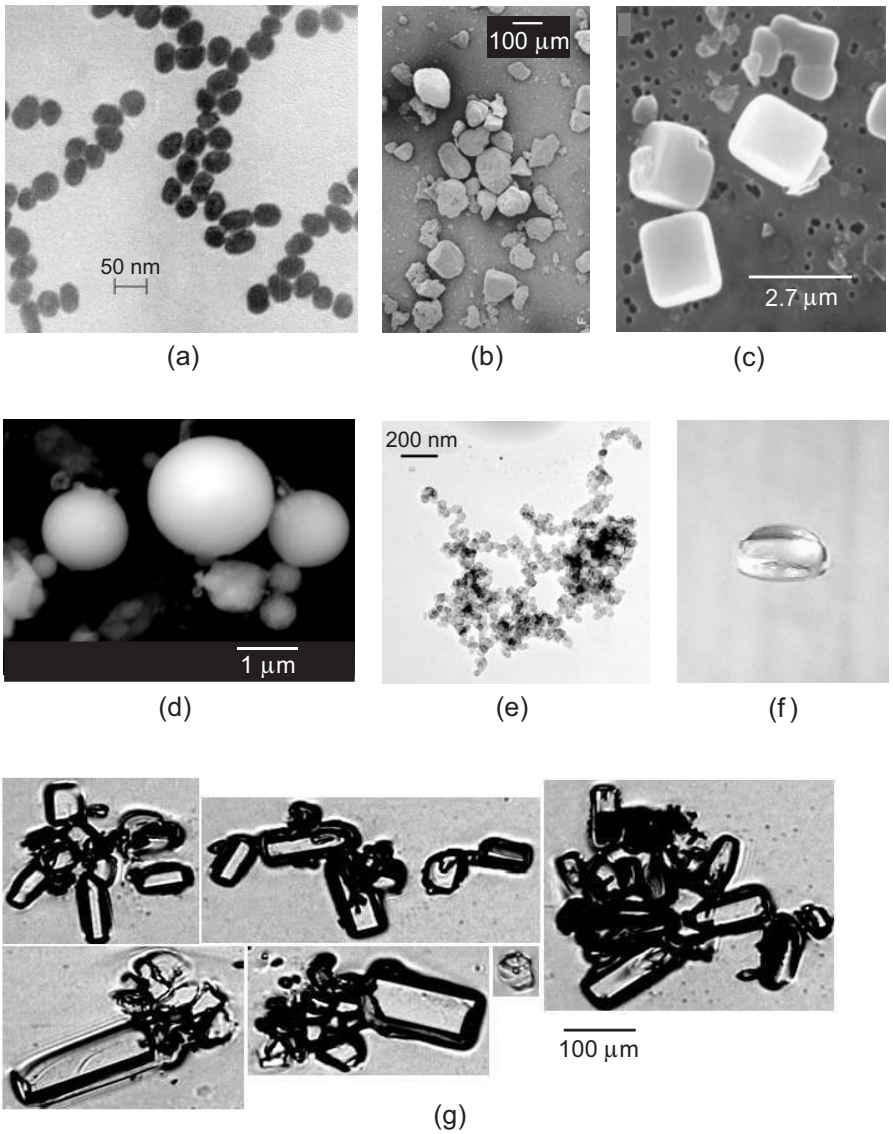

Plate 1.1. Examples of man-made and natural small particles. (a) 40-nm-diameter gold particles (after Khlebtsov et al. 1996). (b) Sahara desert sand (after Volten et al. 2001). (c) Dry sea-salt particles (after Chamaillard et al. 2003). (d) Fly ash particles (after Ebert et al. 2002). (e) A soot aggregate (after Li et al. 2003). (f) A 6-mm-diameter falling raindrop. (g) Cirrus cloud crystals (after Arnott et al. 1994).

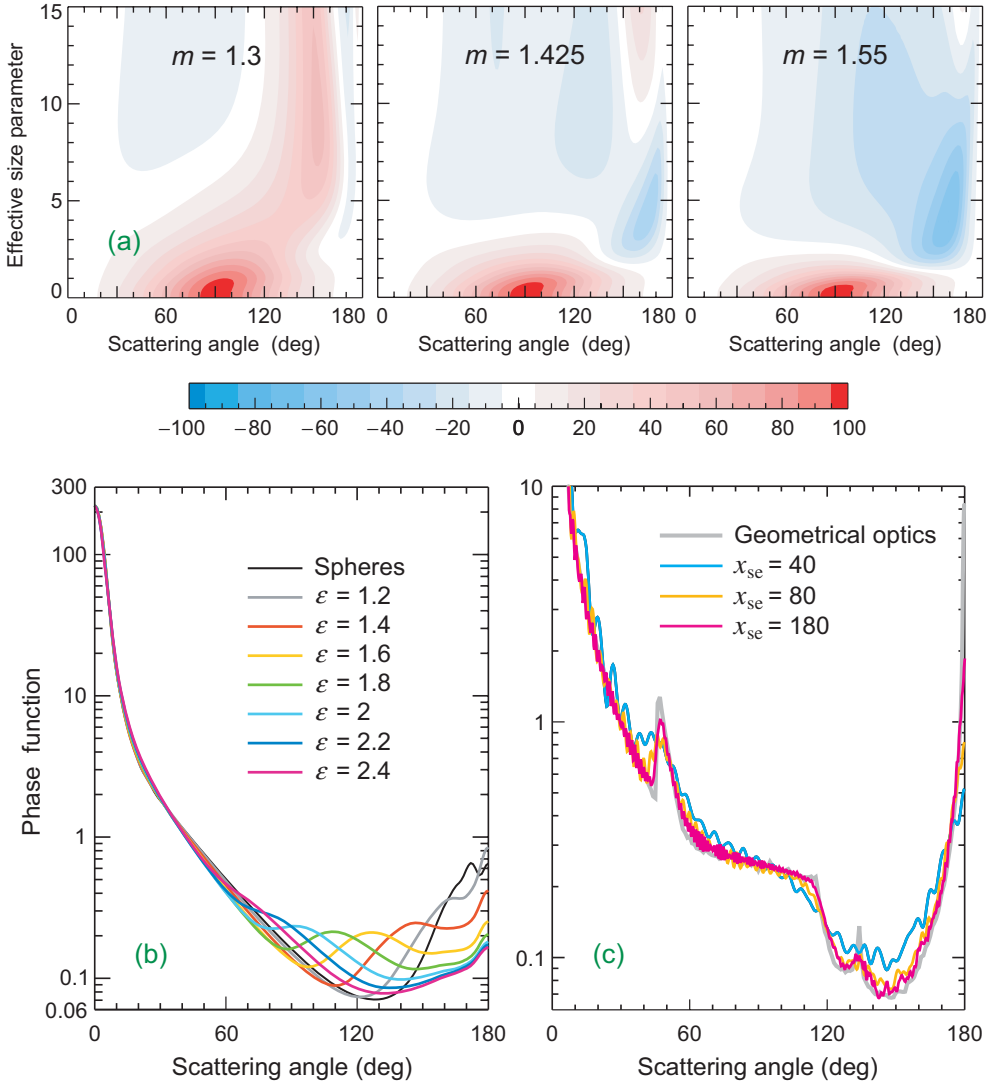

Plate 1.2. (a) Degree of linear polarization for unpolarized incident light (in %) versus scattering angle and effective size parameter for polydisperse spherical particles with relative refractive indices 1.3, 1.425, and 1.55. (b) *T*-matrix computations of the phase function for micrometer-sized polydisperse spheres and randomly oriented surface-equivalent prolate spheroids with aspect ratios ranging from 1.2 to 2.4 at a wavelength of 443 nm. The relative refractive index is fixed at 1.53 + i0.008. (c) Geometrical-optics and *T*-matrix phase functions for monodisperse, randomly oriented circular cylinders with surface-equivalent-sphere size parameters x_{se} = 40, 80, and 180. The relative refractive index is 1.311 + i0.311×10^{-8} and is typical of water ice at visible wavelengths.

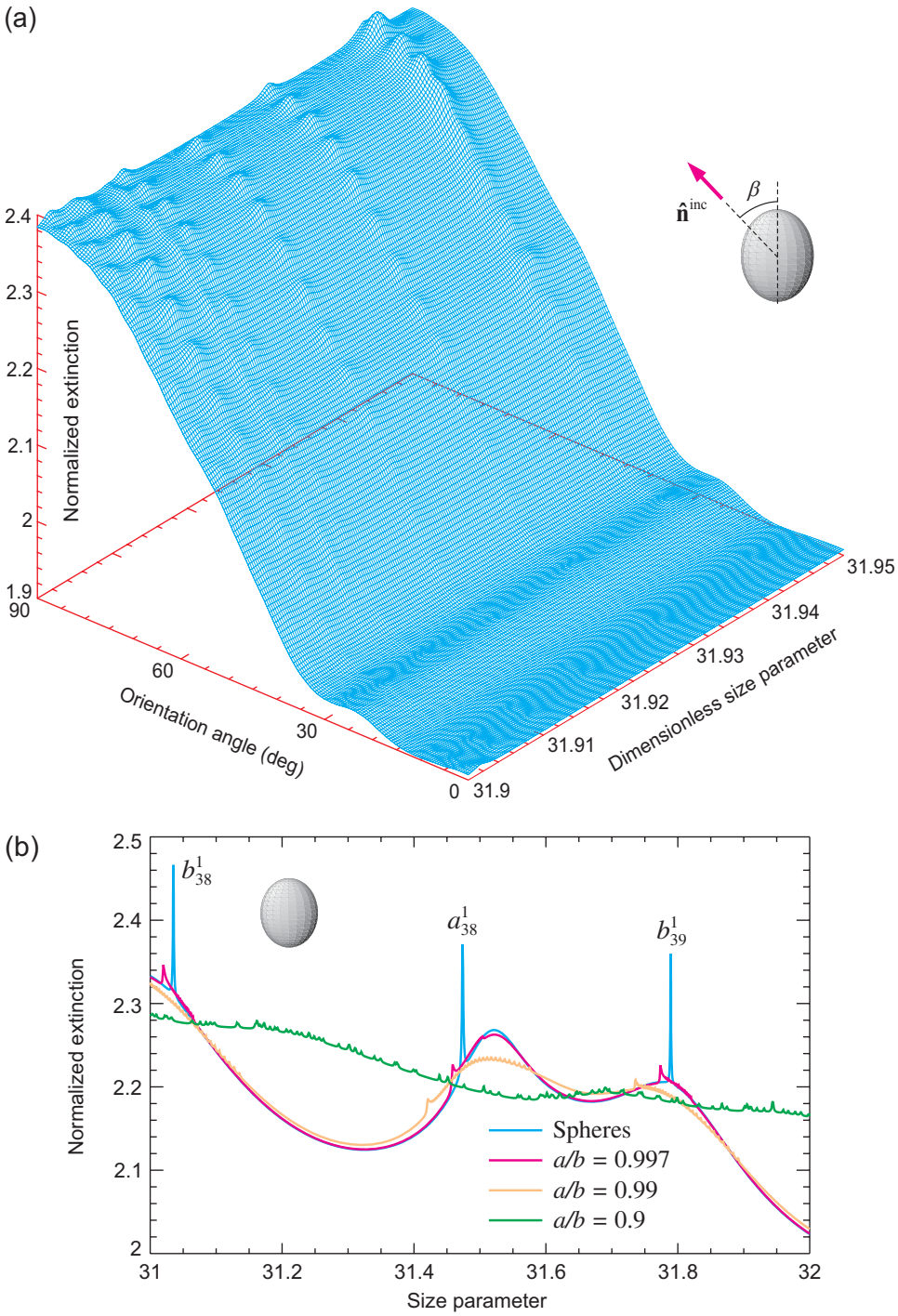

Plate 1.3. (a) Normalized extinction versus x_{ev} and orientation angle for a prolate spheroid with m = 1.4 and a/b = 0.9. (b) Normalized extinction versus x_{ev} for a sphere and a prolate spheroid in random orientation. The results are shown for several values of the spheroid's semi-axis ratio a/b. The relative refractive index is fixed at 1.4.

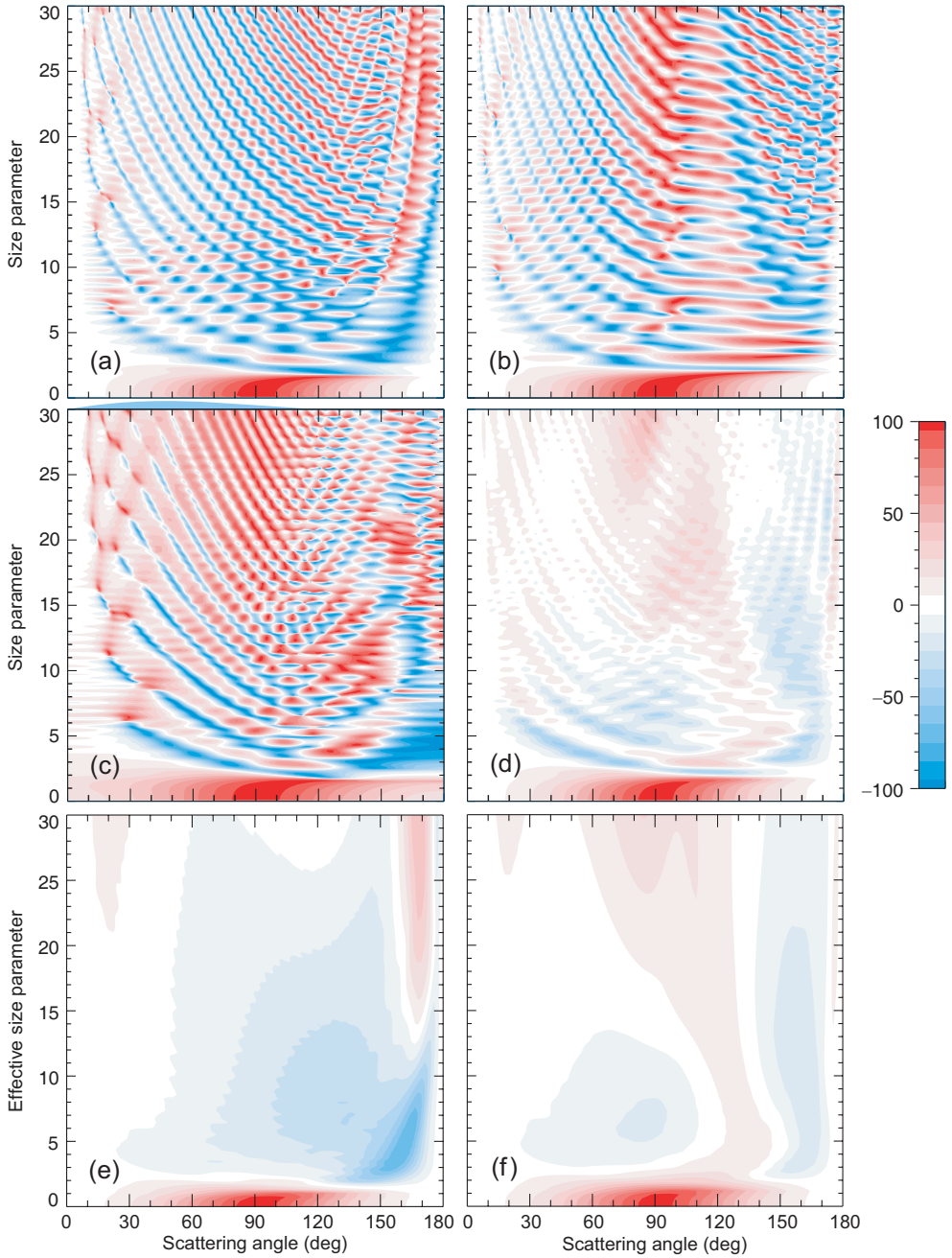

Plate 1.4. (a–c) $-F_{12}/F_{11}$ (in %) versus Θ and x_{se} for a spherical particle (a) and a surface-equivalent oblate spheroid in a fixed orientation (b,c). The rotation axis of the spheroid is oriented along the incidence direction (b) or perpendicularly to the scattering plane (c). (d) $-\langle F_{12}\rangle_\xi/\langle F_{11}\rangle_\xi$ for monodisperse, randomly oriented oblate spheroids. (e,f) $-\langle F_{12}\rangle_\xi/\langle F_{11}\rangle_\xi$ versus Θ and effective surface-equivalent-sphere size parameter for polydisperse spheres and polydisperse, randomly oriented oblate spheroids. The refractive index of all particles is $1.53 + i0.008$ and the spheroid semi-axis ratio is $a/b = 1.7$.

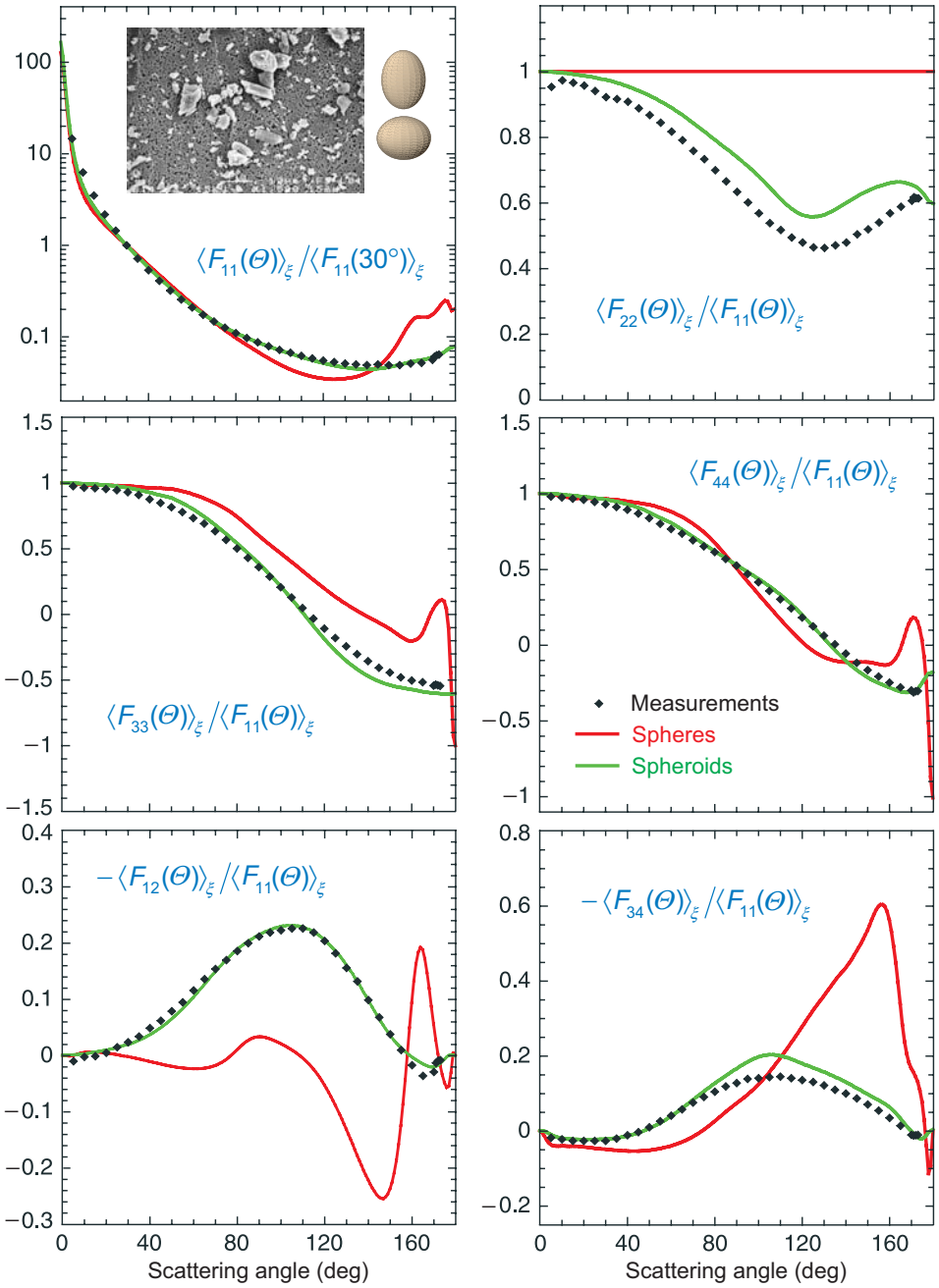

Plate 1.5. Diamonds depict the results of laboratory measurements of the ensemble-averaged scattering matrix for micrometer-sized feldspar particles at a wavelength of 633 nm. The green curves show the result of fitting the laboratory data with *T*-matrix results computed for a shape distribution of polydisperse, randomly oriented prolate and oblate spheroids. The real and model particle shapes are contrasted in the inset. The red curves show the results computed for volume-equivalent polydisperse spherical particles.

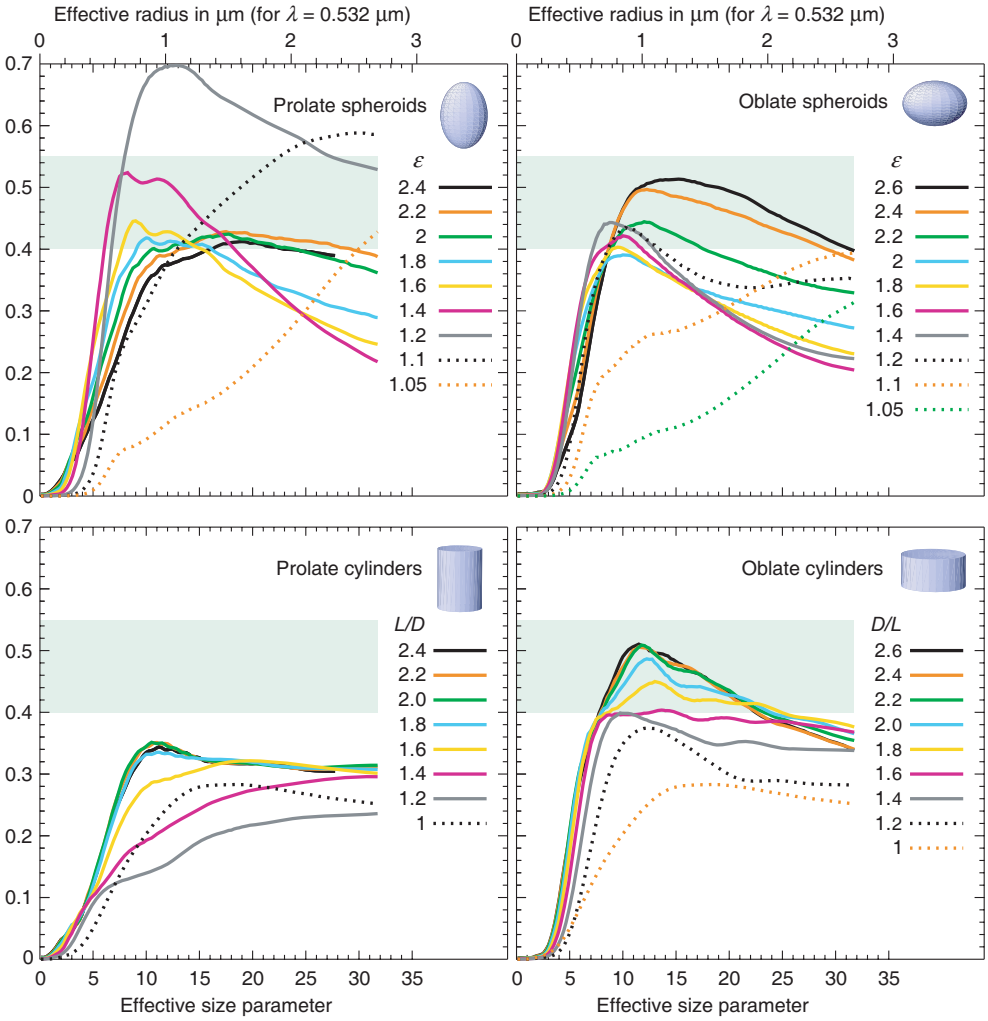

Plate 1.6. Linear depolarization ratio (vertical axes) versus effective surface-equivalent-sphere size parameter for polydisperse, randomly oriented ice spheroids with aspect ratios ranging from 1.05 to 2.6 and circular cylinders with various length-to-diameter or diameter-to-length ratios. The relative refractive index is 1.311. The light-green bands show the range of highest depolarization ratios typically observed for anthropogenic cirrus clouds in the form of aircraft condensation trails (Freudenthaler et al. 1996). The upper horizontal axes convert effective size parameters to effective radii assuming the wavelength $\lambda = 2\pi/k_1 = 0.532$ μm.

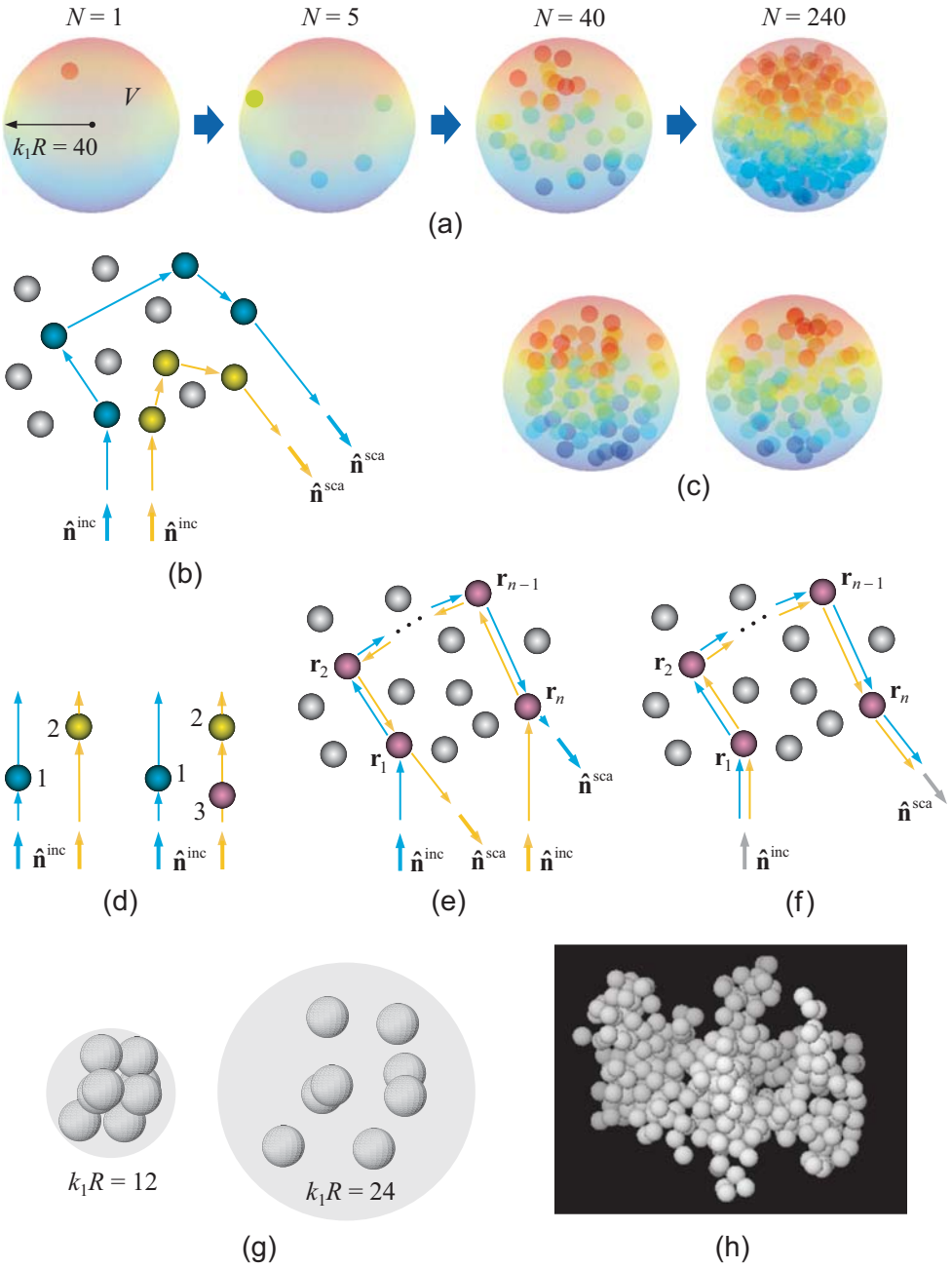

Plate 1.7. (a) Spherical scattering volume V filled with N randomly positioned particles. (b) Interference origin of speckle. (c) Two random realizations of the 80-particle group. (d) Forward-scattering interference. (e) Interference origin of coherent backscattering. (f) Interference origin of the diffuse background. (g) Spherical volumes filled with eight randomly positioned, identical particles. (h) Fractal aggregate composed of 334 identical spherical monomers.

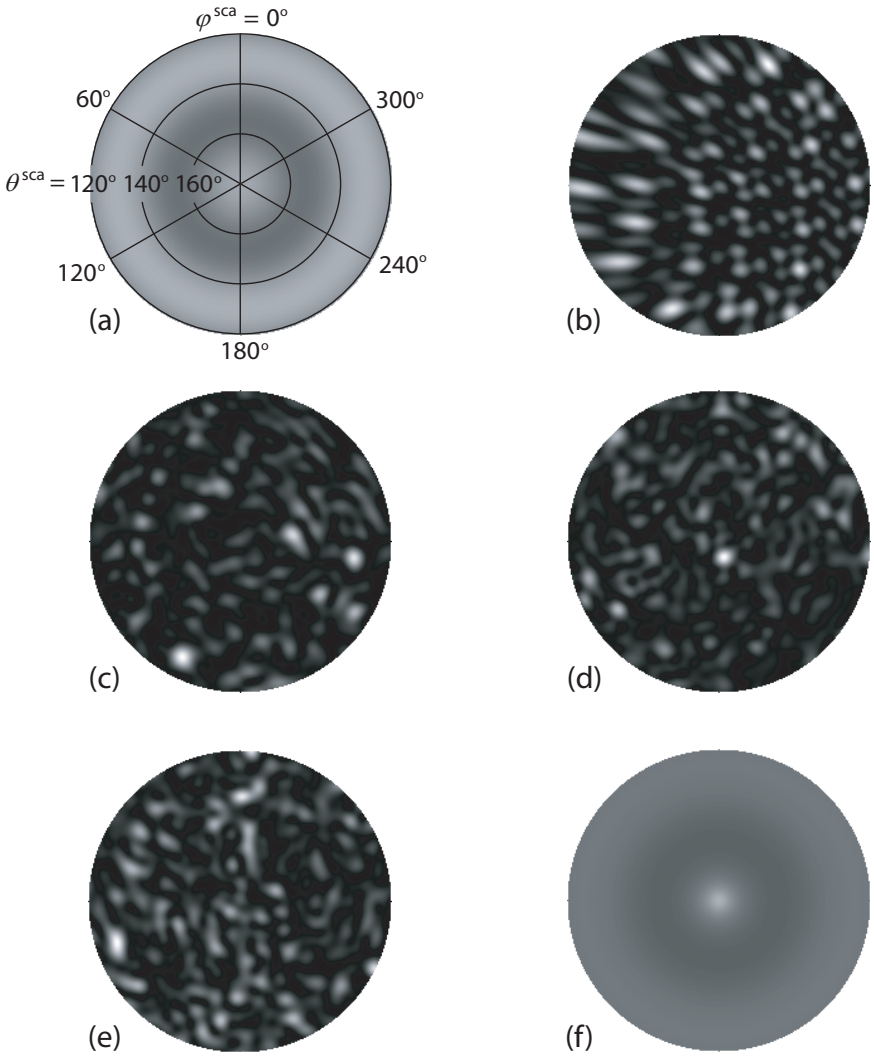

Plate 1.8. Angular distribution of scattered intensity in the far-field zone of the spherical volume V filled with N particles. (a) $N = 1$, fixed orientation. (b) $N = 5$, fixed orientation. (c) $N = 20$, fixed orientation. (d) and (e) $N = 80$, fixed orientation. (f) $N = 80$, random orientation. The gray scale is individually adjusted in order to maximally reveal the details of each scattering pattern. Panel (a) also shows the angular coordinates used for all panels.

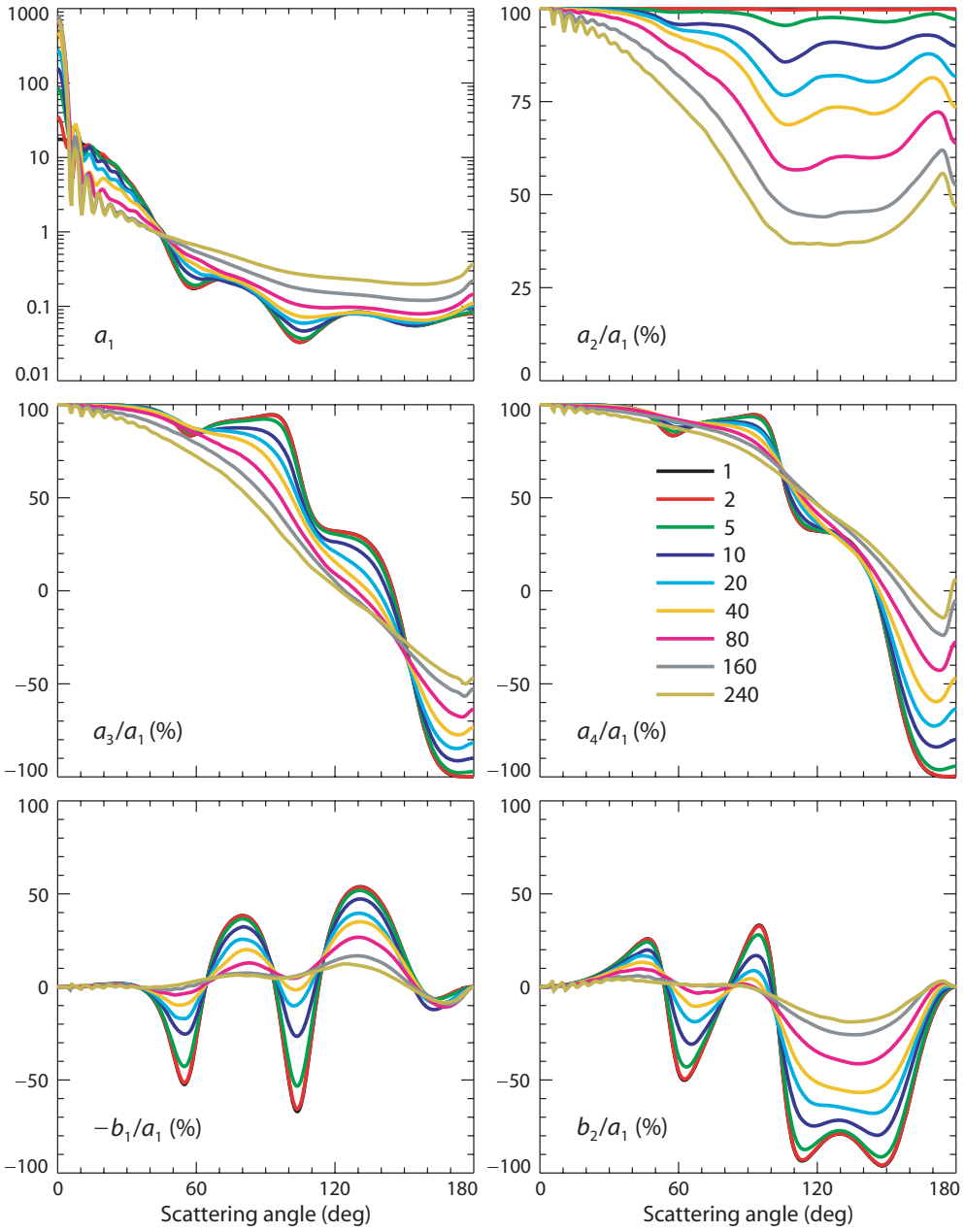

Plate 1.9. Elements of the normalized Stokes scattering matrix computed for a $k_1R = 40$ spherical volume of discrete random medium filled with $N = 1, \ldots, 240$ particles.

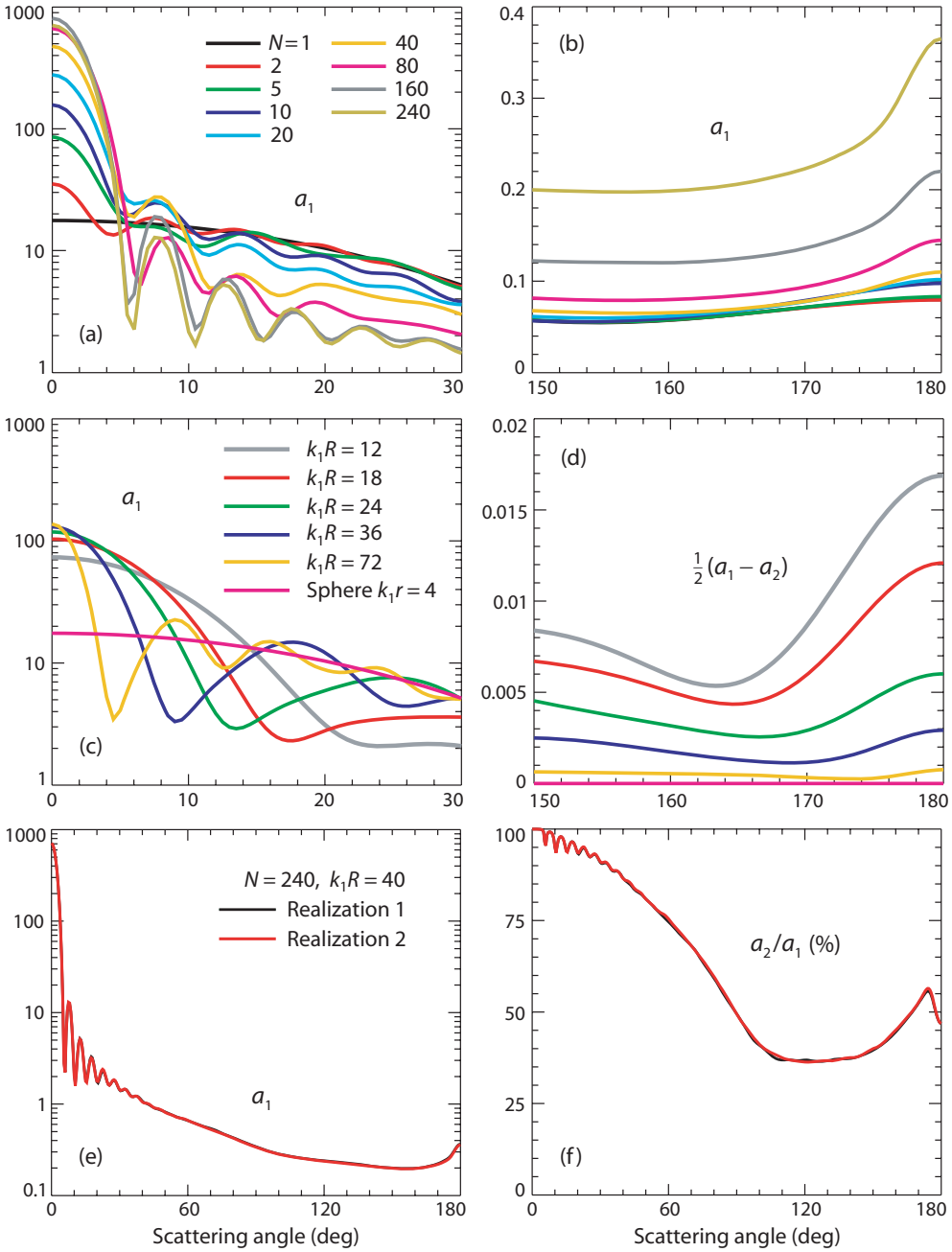

Plate 1.10. Scattering properties of a spherical volume of discrete random medium.

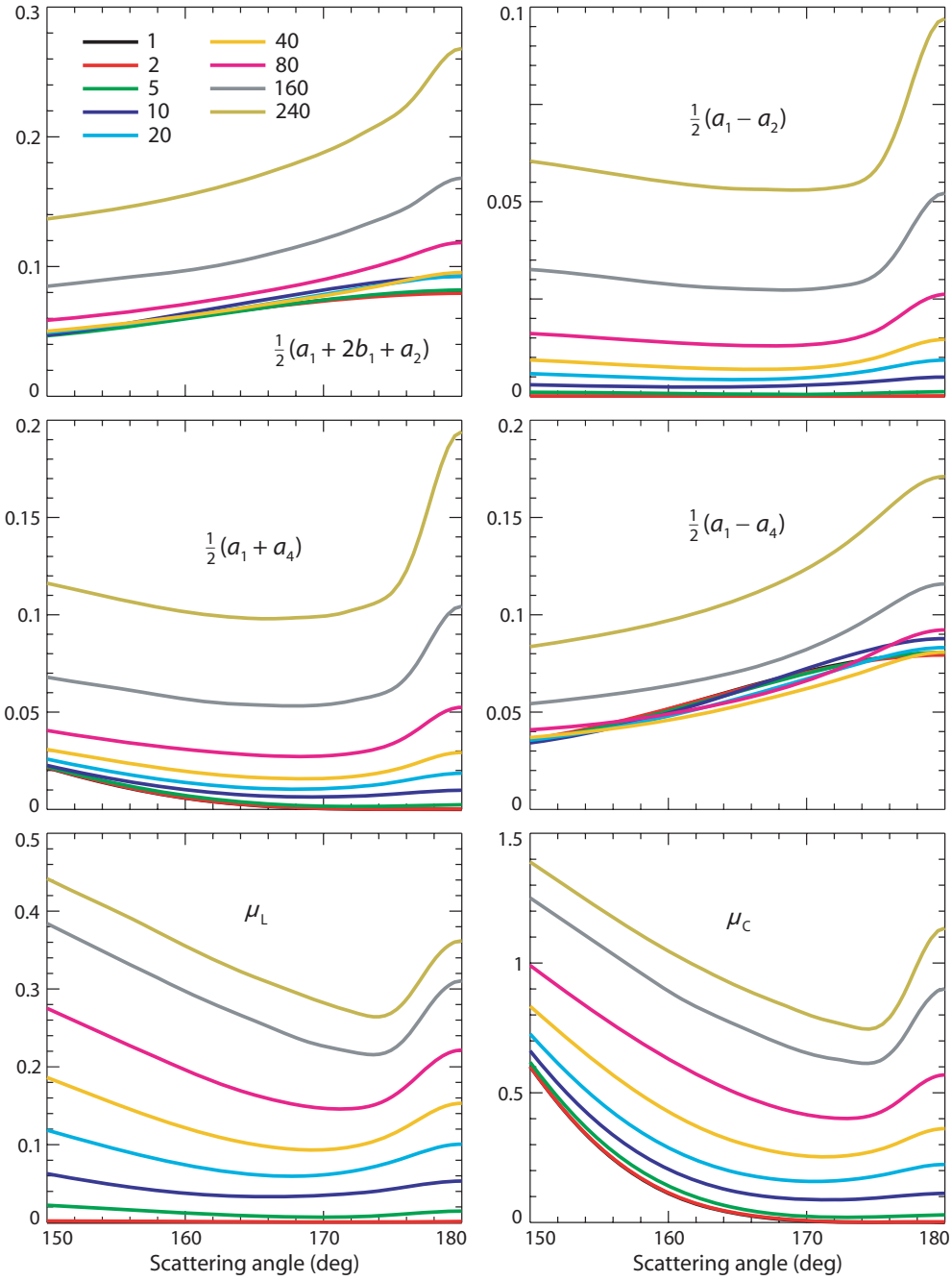

Plate 1.11. Polarization characteristics of backscattered light computed for a $k_1R = 40$ spherical volume of discrete random medium filled with $N = 1, \ldots, 240$ particles.

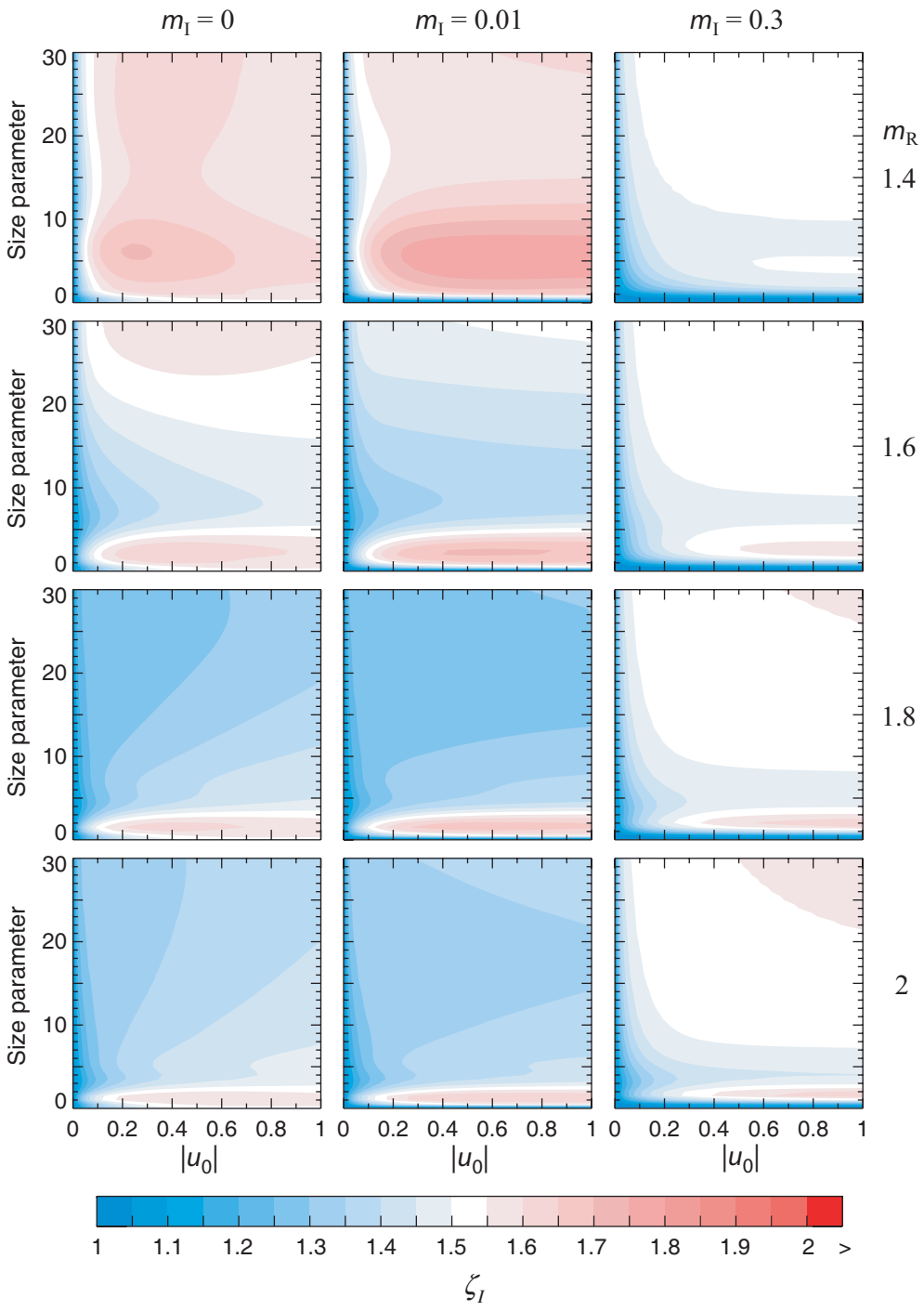

Plate 1.12. Enhancement factor ζ_I.

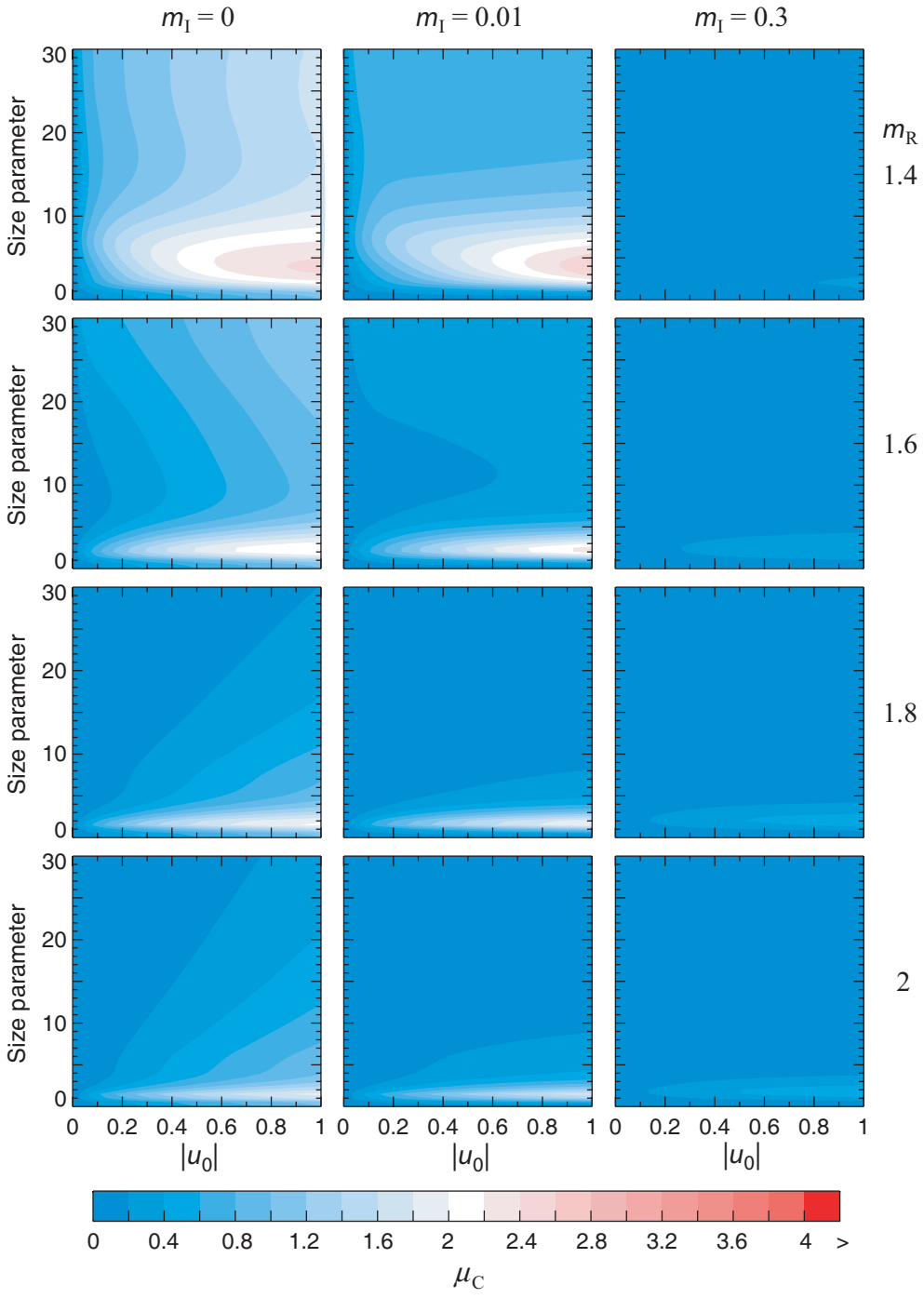

Plate 1.13. Polarization ratio μ_C.

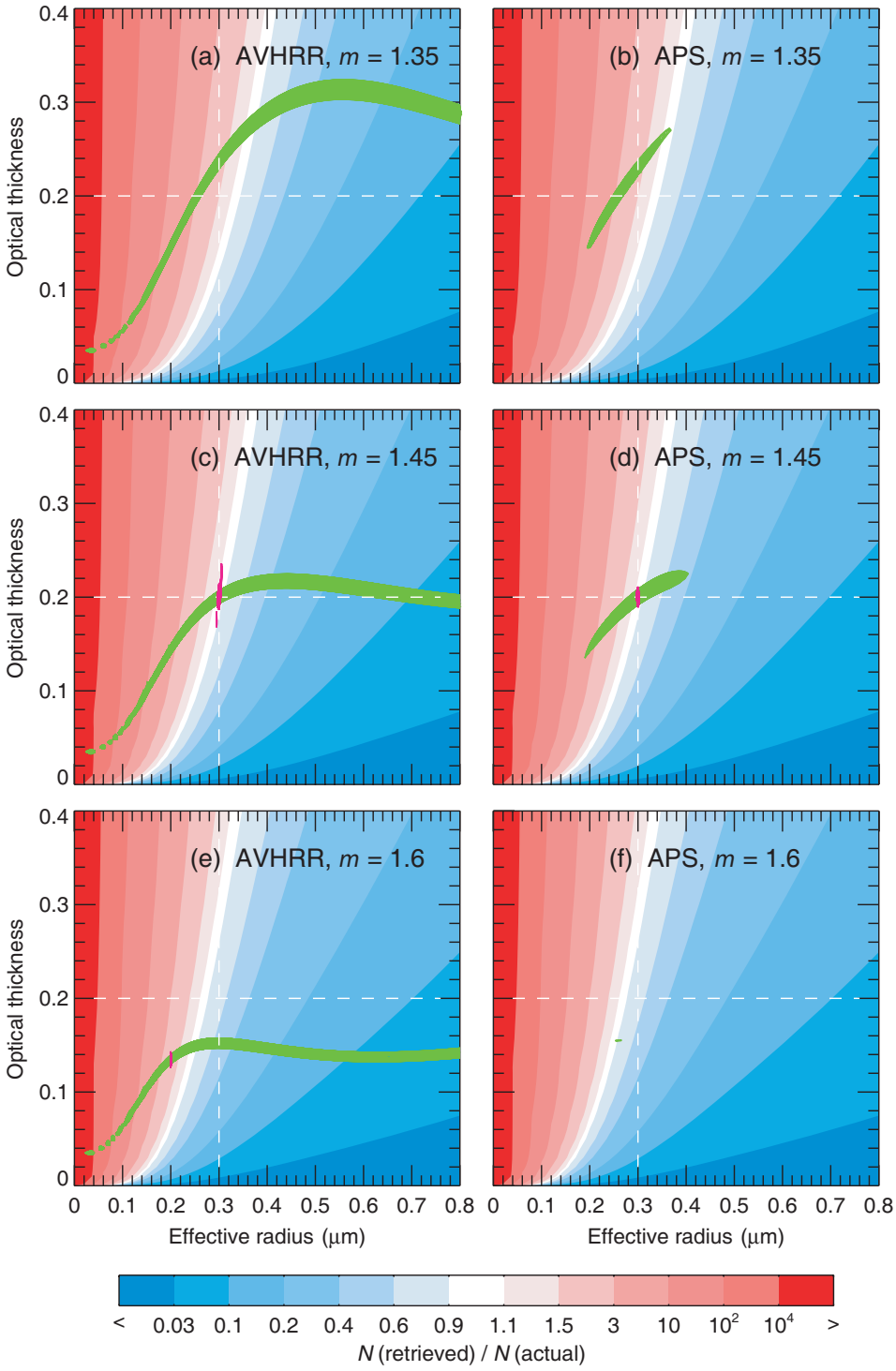

Plate 2.1. Modeling different types of aerosol retrievals (see text).

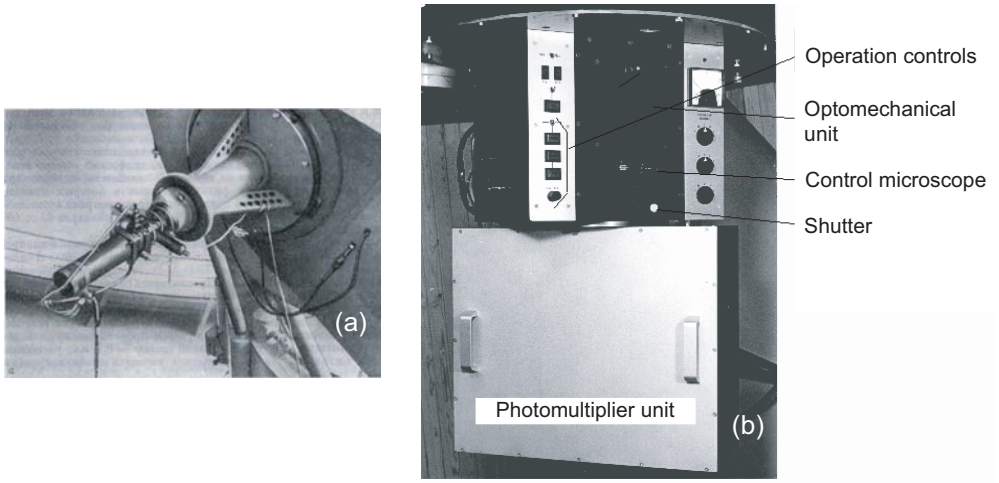

Plate 2.2. (a) The first CrAO polarimeter mounted on the telescope ZTSh. (b) Five-channel photopolarimeter.

Plate 2.3. CrAO telescopes used for photopolarimetric observations.

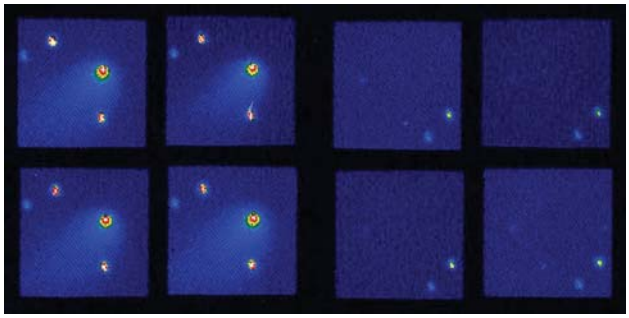

Plate 2.4. Polarization images of comet 21P/Ashbrook–Jackson and the background sky.

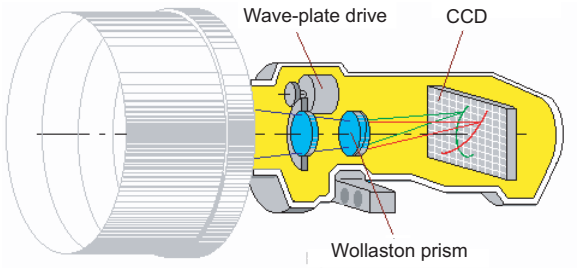

Plate 2.5. Optical scheme of the UV spectropolarimeter with an original Wollaston prism.

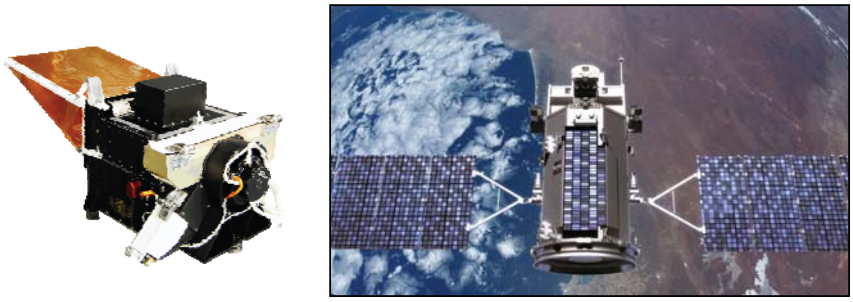

Plate 2.6. Orbital photopolarimeter APS (left) and artist's rendition of the NASA orbital satellite Glory (right).

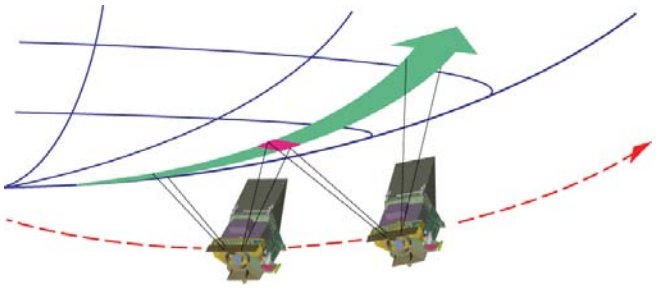

Plate 2.7. Along-track multiangle APS measurements via 360° scanning from the sun-synchronous polar-orbiting Glory spacecraft.

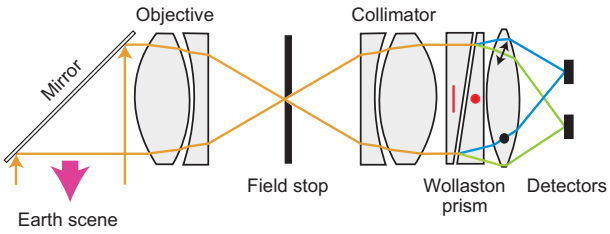

Plate 2.8. APS optical approach for polarization measurement. Red markings show the orientations of the optical axes of the birefringent crystals forming the Wollaston prism. Orange lines show ray paths undergoing the split into orthogonal polarizations as indicated by the green and blue lines.

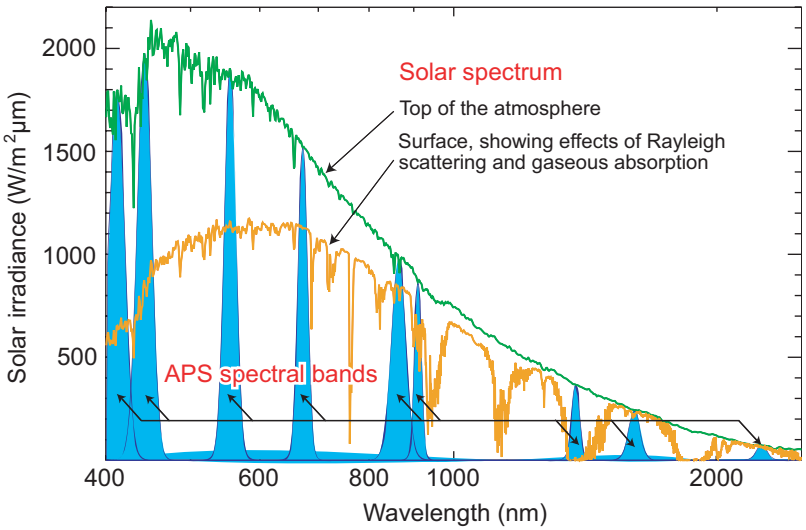

Plate 2.9. Locations of the APS spectral channels.

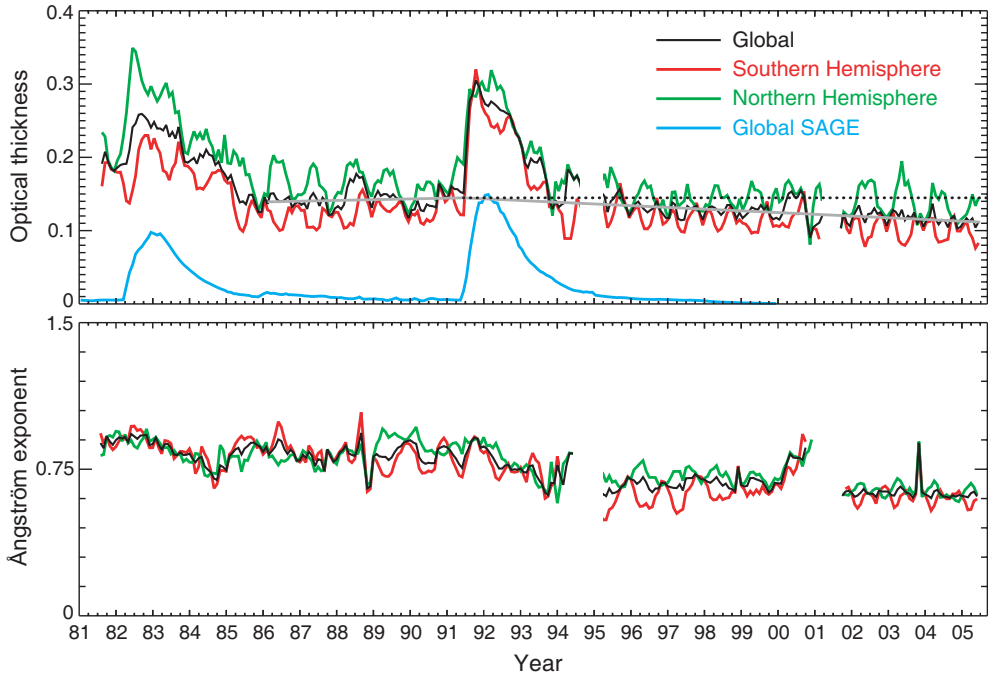

Plate 3.1. Global and hemispherical monthly averages of the AOT and Ångström exponent over the oceans for the period August 1981 – June 2005 derived with the latest version of the GACP retrieval algorithm. The blue curve depicts the SAGE record of the globally averaged stratospheric AOT. The solid grey lines show pre- and post-Pinatubo linear regressions. The black dotted line represents the June 1991 pre-Pinatubo regression level.

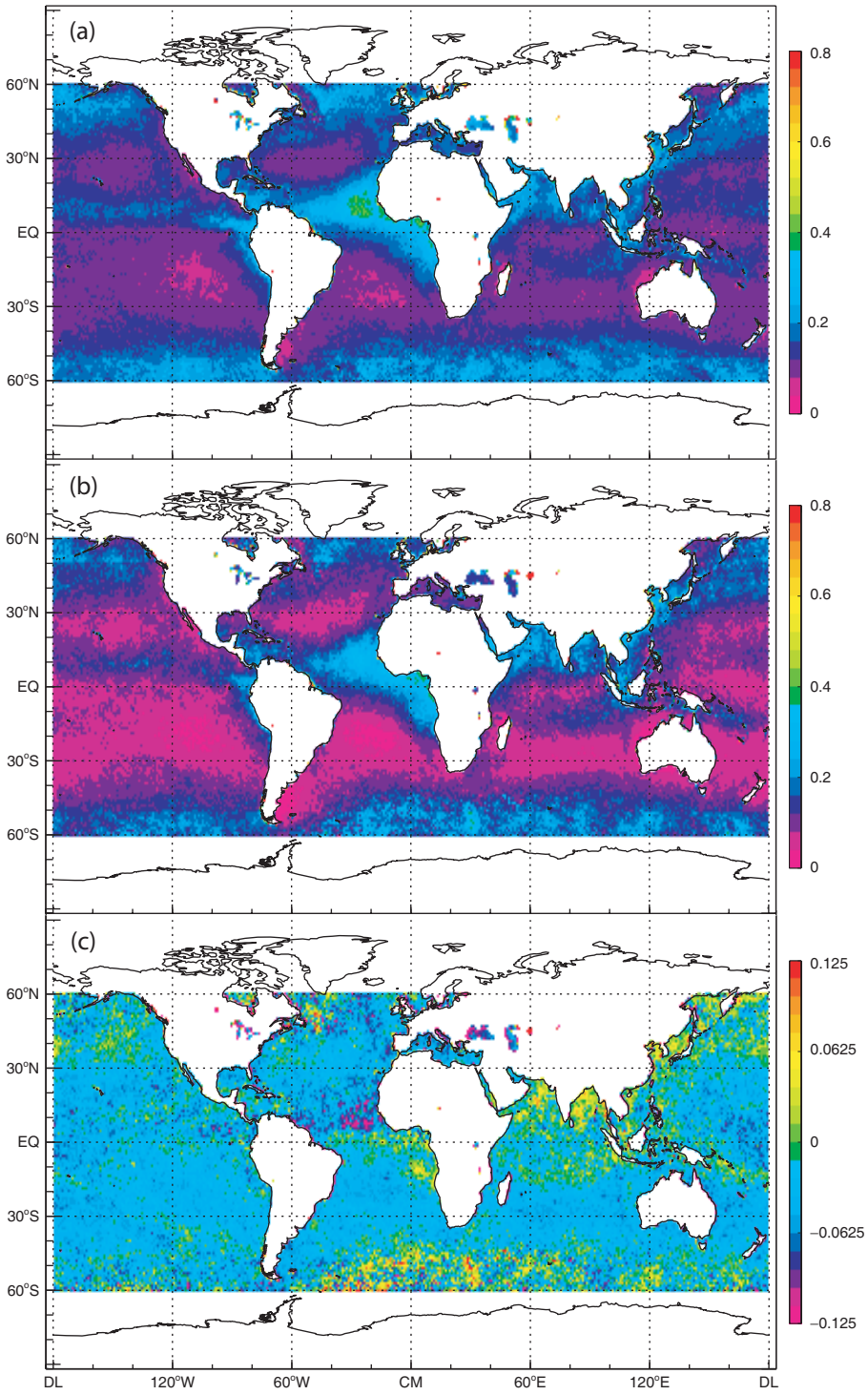

Plate 3.2. (a) AOT averaged over the period July 1988 – June 1991. (b) AOT averaged over the period July 2002 – June 2005. (c) Difference between the AOTs in panels (b) and (a).

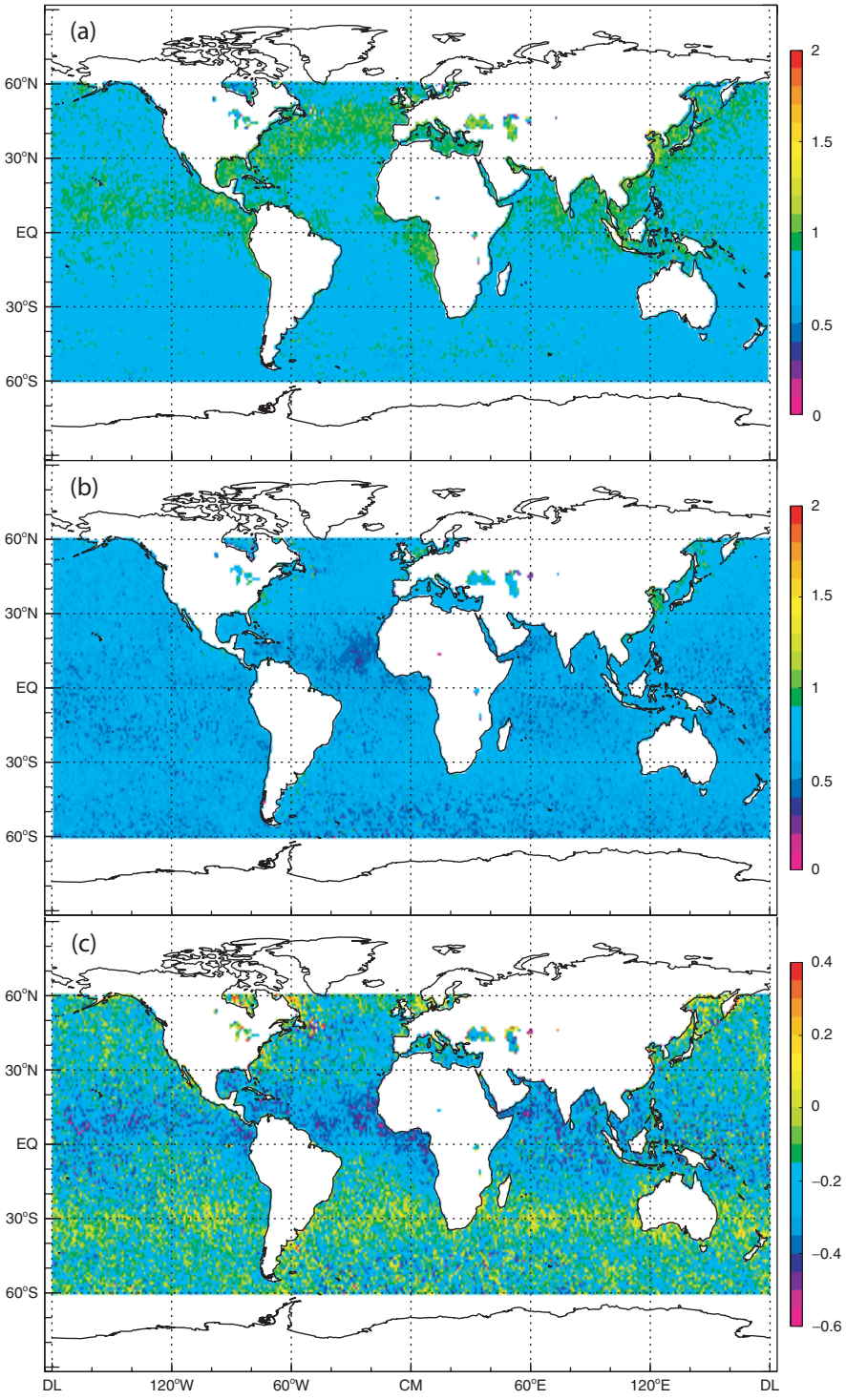

Plate 3.3. Ångström exponent averaged over the periods July 1988 – June 1991 (a) and July 2002 – June 2005 (b). (c) Difference between the Ångström exponents in panels (b) and (a).

Plate 3.4. Polarimeter RSP (left) designed for remote-sensing studies of aerosols and clouds from high-flying NASA aircraft such as the Proteus (right).

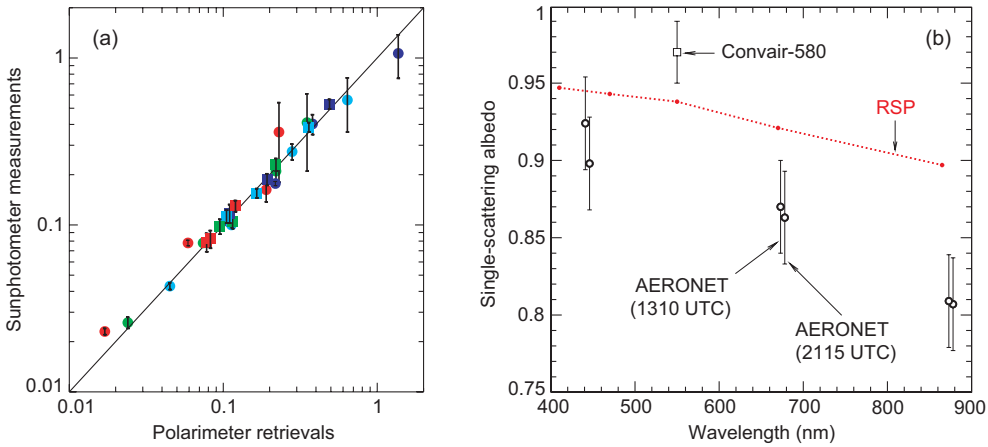

Plate 3.5. (a) Optical thickness comparison. Sunphotometer measurements at 410/443, 500, 673, and 865 nm shown as blue, turquoise, green, and red symbols, respectively, are compared with RSP retrievals for the same wavelength. The circular symbols are for retrievals over land while the square symbols are for retrievals over ocean. Error bars are only shown for the sunphotometer measurements. (b) Single-scattering albedos as a function of wavelength. The red dotted line shows the best-estimate values retrieved from RSP data. Also included are estimates from data collected during Convair-580 flight 1874 and from the AERONET data.

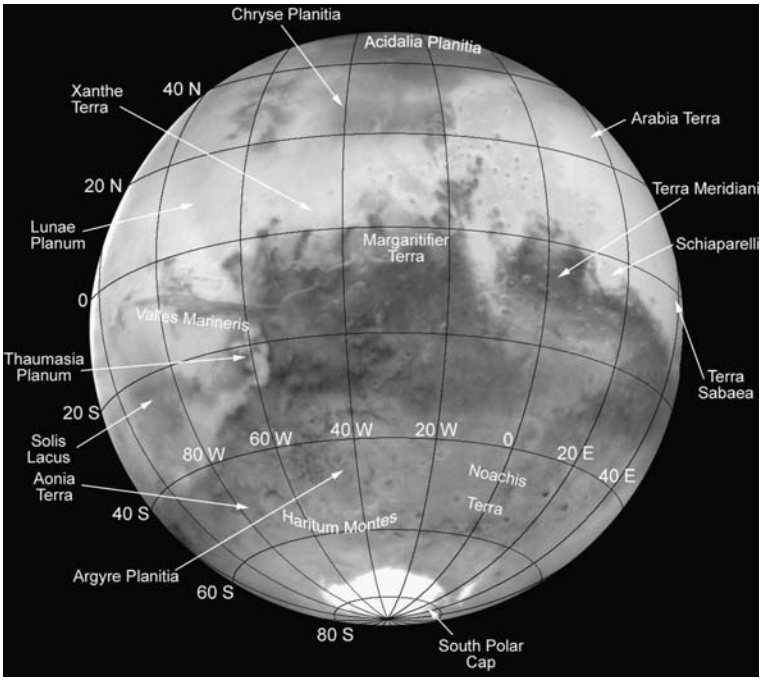

Plate 3.6. The map of the martian hemisphere centered at ~19°S and ~34°W as represented by an image acquired in the red spectral band (filter F658W).

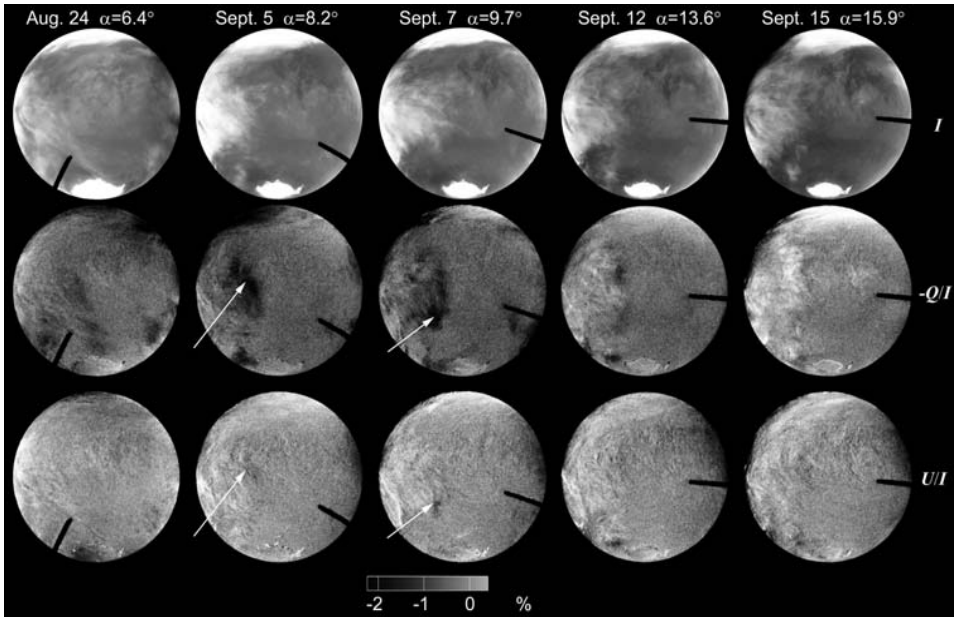

Plate 3.7. Intensity I and ratios $-Q/I$ and U/I for Mars on all five observation dates measured with the filter F330W. The Stokes parameters are defined with respect to the photometric-equator-related reference frame. The black coronographic finger shadows parts of the detector. The arrows indicate the polarimetric transient effect.

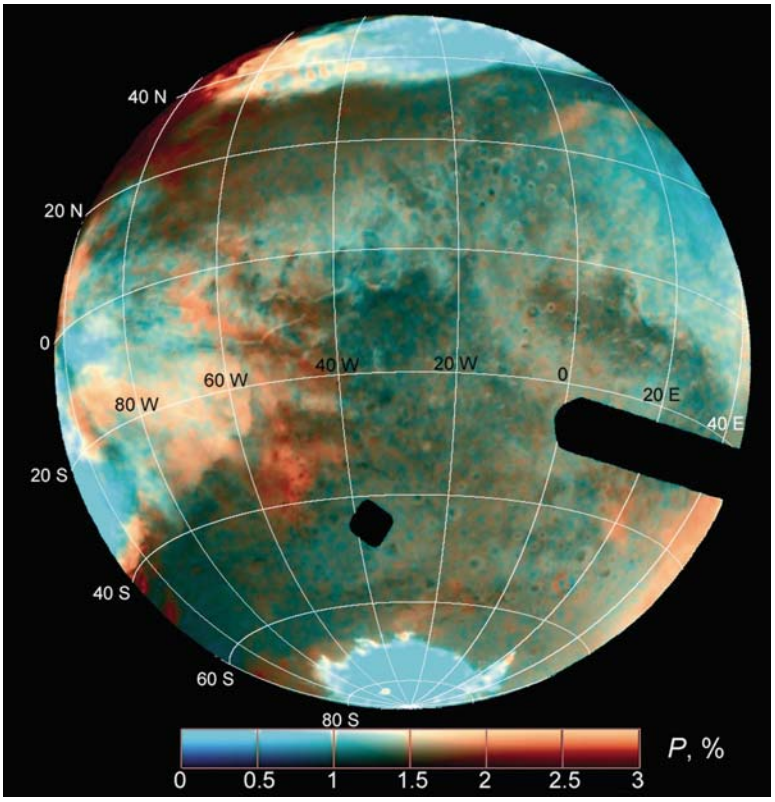

Plate 3.8. Color-coded distribution of the degree of linear polarization $(Q^2+U^2)^{1/2}/I$ over the martian disk is superposed on the brightness image (filter F435W; September 7, 2003).

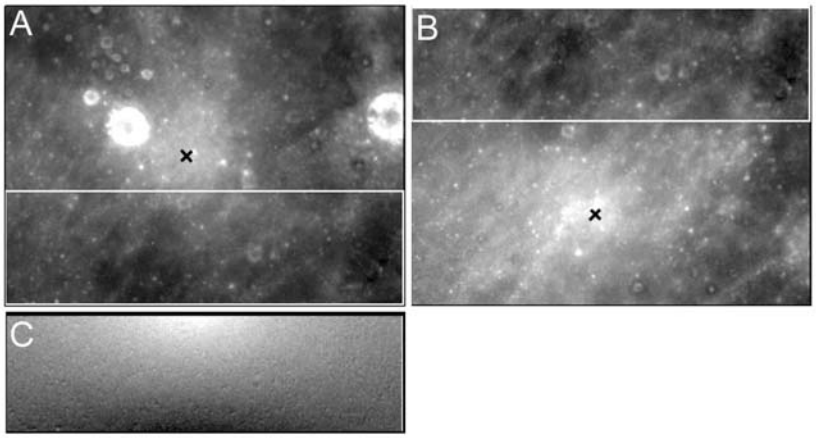

Plate 3.9. Images obtained with the UVVis camera onboard the Clementine spacecraft. The south is above. Craters Bruce and Blagg in the north-eastern part of Sinus Medii are seen in the source image (A). The adjacent part of Sinus Medii is shown in (B). The ratio of the source images (C) reveals a pattern caused by a mutual shift of the opposition spot by ~1°. The crosses denote the opposition point $\alpha = 0°$.

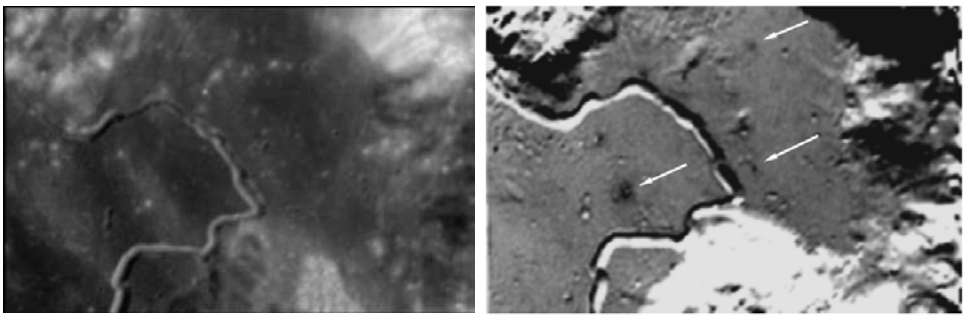

Plate 3.10. (a) Region of the lunar surface surrounding the Apollo-15 landing site. (b) The corresponding map of the phase-function slope distribution. Darker shades represent flatter phase functions. The arrows indicate the most characteristic photometric anomalies.

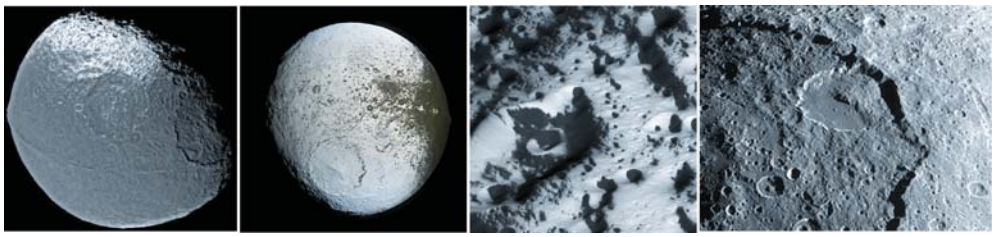

Plate 3.11. The left-hand image shows the trailing hemisphere of Iapetus covered with ancient impact craters. Essentially along the equator one can see a unique geological structure in the form of a mountain ridge which is more that 13 km tall, ~20 km wide, and at least 1,300 km long. The two central images show the distribution of bright and dark materials over the surface of Iapetus. The right-hand image shows a gigantic landslide indicative of the presence of fine-dispersed and porous surface material. The images were obtained from the Cassini spacecraft (courtesy NASA).

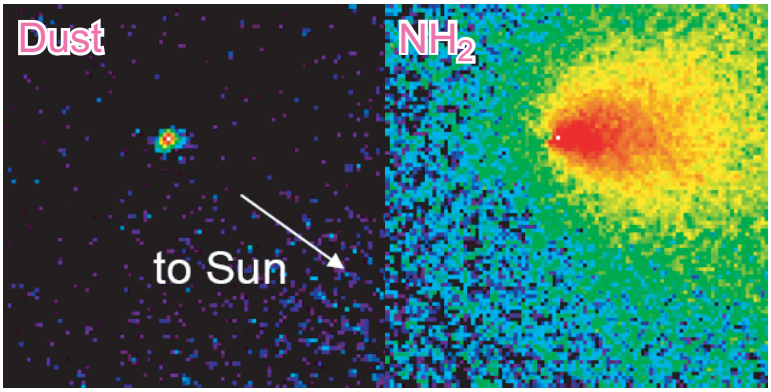

Plate 4.1. Optical images of dust and NH_2 in comet Encke obtained by K. Jockers, T. Bonev, and G. Borisov on the 2-m telescope of the Bulgarian National Astronomical Observatory (Rozhen) on 21 November 2003.

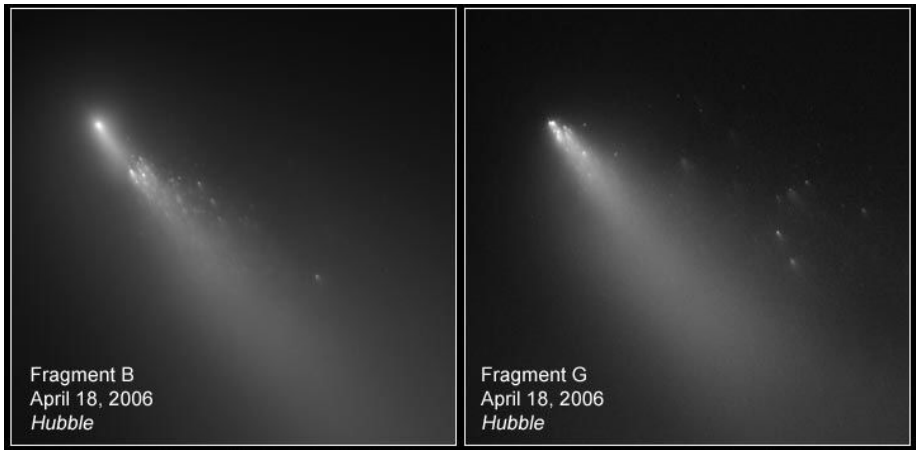

Plate 4.2. HST images documenting the fragmentation of the B and G subnuclei of comet Schwassmann–Wachmann 3 (courtesy NASA).

Plate 4.3. Images of comet Holmes taken on 3 and 27 November 2007 during a superoutburst (http://uk.geocities.com/martinmobberley/Comets.html; courtesy M. P. Mobberley).